RSC Advances

ROYAL SOCIETY OF CHEMISTRY

PAPER

View Article Online
View Journal | View Issue

Check for updates

Cite this: *RSC Adv.*, 2025, **15**, 44218

Synthesis of a C-TiO_2/BiOCl Z-scheme composite photocatalyst for the photocatalytic degradation of tetracycline hydrochloride

Fang-Di Wu, *[a] Shuang Yang,[b] Jyh-Cherng Chen [c] and Ao-xue Fang[b]

Received 11th October 2025
Accepted 6th November 2025

DOI: 10.1039/d5ra07760e

rsc.li/rsc-advances

A composite photocatalyst with enhanced catalytic performance (C-TiO_2/BiOCl) was prepared through a straightforward precipitation–calcination approach. The structural features, photoelectric behavior, morphology, and photocatalytic efficiency of the synthesized materials were studied *via* multiple analytical techniques. Compared with C-TiO_2 and BiOCl, the C-TiO_2/BiOCl composite displayed markedly improved photocatalytic degradation efficiency toward tetracycline hydrochloride (TCH) under simulated solar radiation. The degradation rate of TCH using the 50% C-TiO_2/BiOCl (CTB-50) composite photocatalyst reached 89.9%. The increased photocatalytic efficiency of C-TiO_2/BiOCl was primarily associated with its enhanced efficiency in separating photogenerated electron–hole pairs. A Z-type heterojunction photocatalytic mechanism with a C-layer as a medium was proposed based on UV-vis diffuse reflectance spectroscopy, photoelectrochemical analysis, and PL spectroscopy.

Introduction

With the widespread use of water-soluble antibiotic drugs, the concentration of antibiotics in natural water bodies has continuously increased, facilitating the emergence of antibiotic-resistant bacteria and resistance genes, which pose a severe threat to human health and the ecological environment.[1–3] Tetracycline hydrochloride (TCH), one of the most widely used antibiotics, poses particularly severe hazards because of its resistance to natural degradation and tendency to accumulate.[4] The traditional methods for treating antibiotic wastewater mainly include chemical oxidation, biological treatment, and physical adsorption. However, these processes suffer from issues such as residual chemical reagents and difficulties in post-treatment.[5] Photocatalytic oxidation technology based on semiconductor materials has received increasing attention in the treatment of antibiotic wastewater due to its simple operation, safety, environmental protection, and low cost.[6–8]

Among various semiconductor photocatalysts, bismuth (Bi)-based photocatalysts (such as Bi_2O_3, Bi_2WO_6, Bi_2MoO_6, $BiVO_4$, and BiOX) have recently attracted greater scientific interest for improving the catalytic activity of composite photocatalysts due to their distinctive layered structures, high chemical stability, and ease of preparation.[9] Among these, BiOCl possesses an anisotropic layered structure, in which the layers of $[Bi_2O_2]^{2+}$ are intercalated through Cl^- ions. The formation of an internal electric field between the Cl^- layers and $[Bi_2O_2]^{2+}$ can efficiently separate photoinduced electron–hole pairs, thereby achieving high photocatalytic performance.[10,11] However, the wide bandgap energy (E_g = 3.2–3.6 eV) of pure BiOCl limits its utilization of visible light in practical applications. In addition, rapid carrier recombination in single-semiconductor photocatalysts is another major factor restricting energy conversion efficiency.[12]

Among the various improvement strategies—such as exposing active crystal facets, metal/non-metal doping, constructing semiconductor heterostructures, noble metal surface deposition, and sensitizer modification—the generation of heterostructures (as a strategic approach to overcome the inherent drawbacks of single-component photocatalysts) can effectively facilitate the separation of photogenerated hole/electron pairs and evidently improve their photocatalytic efficiency.[1,13] Consequently, this approach has become a primary technique for enhancing visible light application efficiency.[14]

Song *et al.*[15] fabricated a g-C_3N_4/BiOCl heterojunction composite photocatalyst through a hydrothermal process and examined its ability to decompose rhodamine B (RhB) under irradiation by visible light. The findings revealed a markedly enhanced degradation rate compared with that of pure BiOCl. Similarly, Chang *et al.*[16] synthesized a BiOCl/AgBr heterostructured composite photocatalyst by combining solvothermal and precipitation techniques. Their findings revealed that the 1 : 1 molar ratio-based BiOCl/AgBr composite achieved the highest RhB degradation efficiency under visible light. Compared with those of pristine AgBr and BiOCl, the BiOCl/AgBr composite showed enhanced photocatalytic stability. Wang *et al.*[17,18] prepared 2D/2D $(BiO)_2CO_3$/BiOCl type-II and S-scheme

---

[a] Fujian Provincial Key Laboratory of Eco-Industrial Green Technology, Wuyi University, Wuyishan, China. E-mail: fangdi4666@sina.com

[b] School of Ecological and Resources Engineering, Wuyi University, Wuyishan, China

[c] Department of Environmental Engineering and Science, Feng Chia University, Taichung, Taiwan

heterojunction catalysts, respectively, which exhibited catalytic activities for TCH that were 5.2 and 20.8 times greater than those of pure $(BiO)_2CO_3$. Ding *et al.*[19] fabricated a Bi/BiOI/BiOCl Z-scheme heterojunction photocatalyst and investigated its catalytic activity toward tetracycline.

Previous studies have shown that carbon-doped (C-doped) TiO_2 can generate intermediate energy levels between the valence and conduction bands of TiO_2. These intermediate levels serve as transition states for photogenerated electron migration, effectively reducing the energy required for migration and thereby extending absorption into the visible light region.[20,21] $Ti_3C_2T_x$ MXenes, novel 2D transition metal carbides, are characterized by a mature preparation process, low cost, non-toxicity, excellent electrical conductivity, a favorable layered structure, and a tunable bandgap.[22,23] Moreover, $Ti_3C_2T_x$ inherently contains a carbon source. During the oxidation process of synthesizing TiO_2 from $Ti_3C_2T_x$, the incorporated carbon acts as a dopant in TiO_2 without requiring external carbon sources. The resulting C-doped TiO_2 (C-TiO_2) is expected to retain the $Ti_3C_2T_x$ 2D lamellar structure, thereby increasing its suitability for photocatalytic reactions.[24]

This study employed $Ti_3C_2T_x$ as the raw material for the fabrication of C-TiO_2 through a facile one-step calcination approach without additional carbon sources. Considering the promising properties of BiOCl and the previously reported superior photocatalytic activity of BiOCl/TiO_2 composites,[14,25] this work synthesized BiOCl and C-TiO_2/BiOCl composite photocatalysts *via* a precipitation–calcination approach and applied them to the photocatalytic decomposition of TCH.

Experimental section

Preparation of C-TiO_2

C-TiO_2 was prepared by calcining 0.2 g of MXene–$Ti_3C_2T_x$ (purity of 99 wt%, Beijing Beike New Material Technology Co., Ltd, China) in a muffle furnace for 2.5 h at 400 °C. The C-TiO_2 powder was extracted after it was cooled to ambient temperature.

Preparation of BiOCl

BiOCl was prepared *via* co-precipitation at room temperature by reacting a bismuth salt (0.01 mol of $Bi(NO_3)_3\cdot 5H_2O$, AR, Sinopharm Chemical Reagent Co., Ltd, China) with a chlorine source (0.012 mol of KCl, GR, Sinopharm Chemical Reagent Co., Ltd, China) in a nitric acid solution (25 mL, 2 M).[14] The resulting precipitate was subjected to calcination for 2.5 h at 400 °C (ramp rate = 5 °C min^{-1}). After natural cooling, the BiOCl powder was collected.

Preparation of the C-TiO_2/BiOCl composite photocatalyst

First, 0.01 mol of $Bi(NO_3)_3\cdot 5H_2O$ was mixed with HNO_3 (25 mL, 2 M). Under vigorous stirring, an aqueous solution of KCl (Cl/Bi molar ratio = 1.2) was introduced into the solution of $Bi(NO_3)_3\cdot 5H_2O$. Subsequently, $Ti_3C_2T_x$ was introduced while continuous stirring was maintained. Following 2 h of reaction, the obtained precipitate was subjected to filtration, cleaned with distilled water, and subsequently dried. This was then followed by calcination for 2.5 h at a temperature equal to 400 °C (5 °C min^{-1} heating rate). Upon natural cooling, the C-TiO_2/BiOCl powder was collected. By varying the amount of $Ti_3C_2T_x$ added, C-TiO_2/BiOCl photocatalysts with different ratios were obtained. In this study, the photocatalysts were labeled CTB-*X* (*X*, in this case, indicates the mass ratio of C-TiO_2 to BiOCl, with $X = 10\%$, 30%, 50%, and 70%; CTB denotes C-TiO_2/BiOCl, similarly hereinafter).

Characterization of the materials

The X-ray diffraction data of the prepared materials were measured on a Bruker D8 Advance X-ray diffractometer (XRD) using Cu Kα radiation. The morphology and crystal planes of the materials were measured using TESCAN VEGA3 scanning electron microscopy (SEM) and FEI Talos F200S high-resolution transmission electron microscopy (HRTEM), respectively. The composition and valence states of the elements in the prepared materials were measured *via* X-ray photoelectron spectroscopy (XPS) with a Thermo Scientific K-Alpha+ instrument. The specific surface areas of the prepared materials were recorded on a Quantachrome Autosorb IQ-MP surface area analyzer. The ultraviolet visible diffuse reflectance (UV-vis DRS) spectra and photoluminescence (PL) analysis were performed on a Thermo Fisher Evolution 220 and an Edinburgh transient fluorescence spectrometer with an excitation wavelength of 320 nm (FLS1000), respectively. The photocurrent and electrochemical impedance spectroscopy (EIS) tests were conducted on a CHI660E electrochemical working station, and the testing method was the same as that used in previous research.[26]

Results and discussion

Crystal phase analysis of the C-TiO_2/BiOCl composites

XRD analysis was conducted on the MXene–$Ti_3C_2T_x$, C-TiO_2, BiOCl, and C-TiO_2/BiOCl composites to determine their primary crystal phase structures, and the results are presented in Fig. 1. Following the calcination process, $Ti_3C_2T_x$ exhibited typical

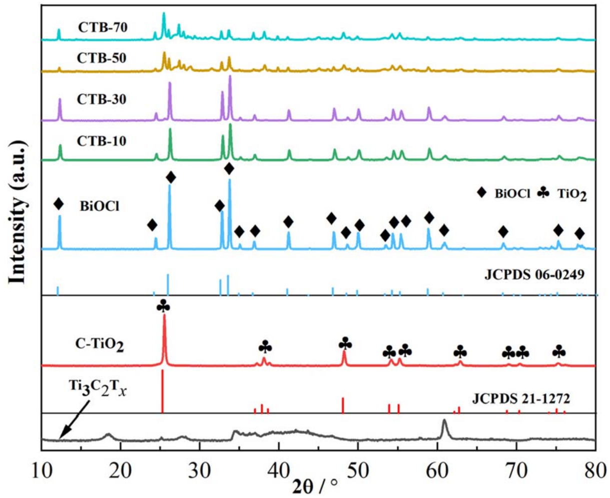

Fig. 1 XRD profiles obtained for the MXene–$Ti_3C_2T_x$, C-TiO_2, BiOCl, and C-TiO_2/BiOCl composites.

signals of anatase TiO_2 at 25.6°, 48.2°, 38.1°, 54.1°, 62.8°, 55.2°, 68.9°, 75.2°, and 70.3°, respectively, ascribed to the planar directions (101), (200), (004), (105), (204), (211), (116), (215), and (220) (JCPDS 21-1272).[27] This confirms that the product obtained after calcination was anatase TiO_2.

The prepared BiOCl samples exhibited characteristic peaks at 12.3°, 24.4°, 26.2°, 32.8°, 33.8°, 35.1°, 36.9°, 41.2°, 46.9°, 48.6°, 50.1°, 53.5°, 54.4°, 55.4°, 58.9°, 60.9°, 68.3°, 75.3°, and 77.8°, corresponding to the (001), (002), (101), (110), (102), (111), (003), (112), (200), (201), (113), (202), (211), (104), (212), (114), (220), (214), and (310) planes, respectively (JCPDS 06-0249). No additional impurity signals were observed, confirming the successful preparation of relatively pure tetragonal BiOCl.[28–30] After the BiOCl/C-TiO_2 composite formed, when the proportion of C-TiO_2 was low, the characteristic peaks of TiO_2 were not prominent, and no significant peak shifts were observed for

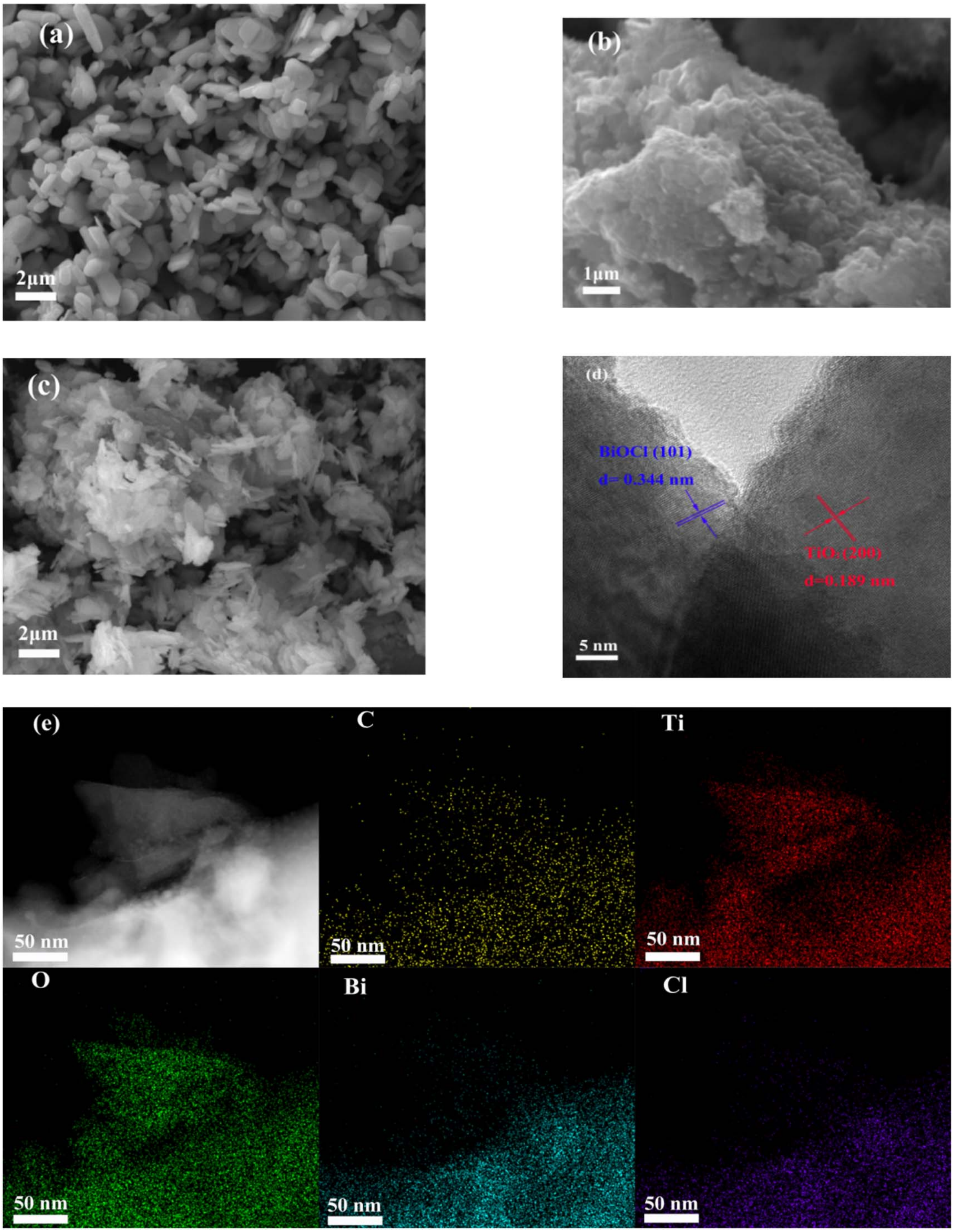

Fig. 2 (a) SEM image of BiOCl, (b) C-TiO_2, (c) and the CTB-50 composite, (d) HRTEM image of the CTB-50 composite, and (e) elemental mapping (C, Ti, O, Bi, Cl) of the CTB-50 composite.

either BiOCl or TiO_2, suggesting that the crystal structures remained intact following composite formation.

Morphological characterization of the C-TiO_2/BiOCl composites

HRTEM and SEM images of BiOCl, C-TiO_2, and the CTB-50 composite material are provided in Fig. 2. As illustrated in Fig. 2(a), pure BiOCl displayed a smooth, regular, and relatively uniform nanosheet structure.[31] After calcination at 400 °C, $Ti_3C_2T_x$ retained its layered structure, with uniformly distributed particles visible on its previously smooth surface. Based on XRD analysis, these particles were identified primarily as carbon-doped anatase TiO_2 (Fig. 2(b)).

Upon compositing BiOCl with C-TiO_2, BiOCl formed finer flakes that were uniformly dispersed and coated onto the surface of C-TiO_2 because of the larger layered structure of C-TiO_2 (Fig. 2(c)). Zhou *et al.*[32] reported that reducing the crystal size and thickness of BiOCl could enhance the catalytic activity during photodegradation. The HRTEM image of the CTB-50 composite is shown in Fig. 2(d). The lattice fringe spacing of 0.189 nm was attributed to the planar direction (200) of TiO_2, whereas the spacing of 0.344 nm was attributed to the planar direction (101) of BiOCl. This confirmed the successful preparation of a C-TiO_2/BiOCl heterojunction composite through the coprecipitation–calcination method. The elemental mapping of CTB-50 (Fig. 2(e)) clearly shows the homogeneous distribution of O, Ti, C, Bi, and Cl, confirming the successful integration of C-TiO_2 and BiOCl.

XPS analysis of the C-TiO_2/BiOCl composites

The electronic states of the CTB-50 composite were determined *via* XPS, and the results are presented in Fig. 3. The XPS survey spectrum (see Fig. 3(a)) revealed distinct binding energy peaks for Ti, C, O, Bi, and Cl.

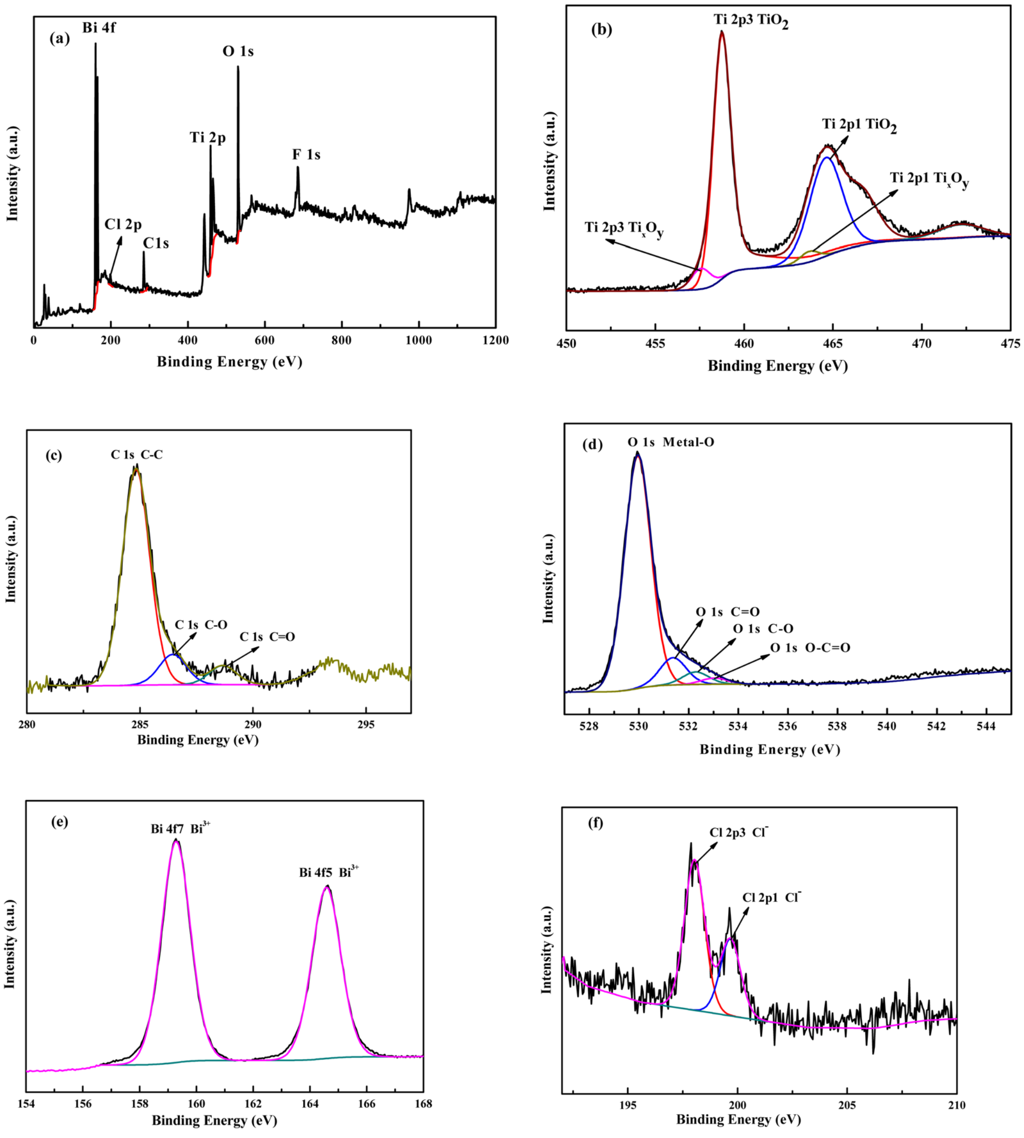

Fig. 3 XPS profiles obtained for the CTB-50 composite: (a) survey, (b) Ti 2p, (c) C 1s, (d) O 1s, (e) Bi 4f, and (f) Cl 2p.

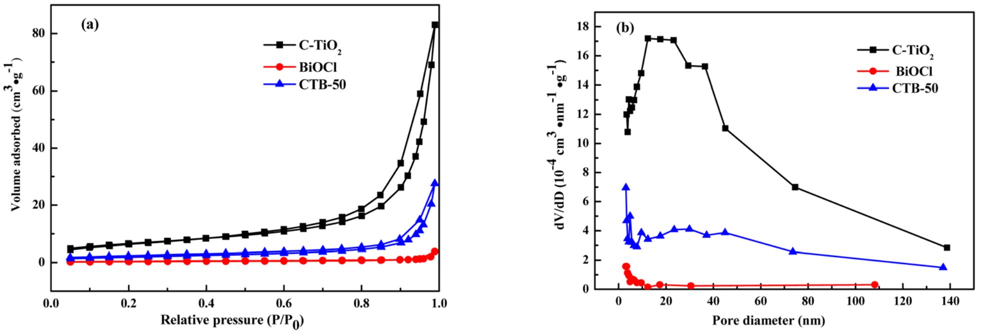

Fig. 4 (a) N_2 desorption/adsorption isotherms and (b) Barrett–Joyner–Halenda (BJH) pore size distribution plots obtained for the C-TiO_2, BiOCl, and CTB-50 composites.

Table 1 BET surface area and pore size of the C-TiO_2/BiOCl composites

Material	Specific surface area (m^2 g^{-1})	Pore size (nm)
C-TiO_2	23.285	12.388
BiOCl	1.334	3.055
CTB-50	6.836	3.057

The Ti 2p spectrum (high-resolution) presented in Fig. 3(b) revealed binding energy signals at 458.78 (Ti $2p_{3/2}$) and 464.68 eV (Ti $2p_{1/2}$), which were attributed to TiO_2 after the calcination of $Ti_3C_2T_x$.[33,34] Additional signals at 463.83 (Ti $2p_{1/2}$) and 457.63 eV (Ti $2p_{3/2}$) were attributed to a small amount of reduced Ti species (Ti_xO_y).[33–35] The C 1s spectrum (see Fig. 3(c)) revealed signals at 284.83 (C–C),[36] 286.46 (C–O),[36] and 288.67 eV (C═O).[37] After calcination, most Ti–C bonds disappeared, with carbon mainly present as C–O and C═O, indicating successful doping into TiO_2.

The signal at 529.95 eV within the O 1s spectrum (Fig. 3(d)) corresponded to metal–O bonds,[38] whereas the signals at 531.37, 532.27, and 533.03 eV were assigned to the C═O group,[39] C–O group,[40] and O–C═O group,[39] respectively.

The Bi 4f spectrum (see Fig. 3(e)) revealed signals at 159.28 (Bi $4f_{7/2}$) and 164.58 eV (Bi $4f_{5/2}$), which were attributed to the

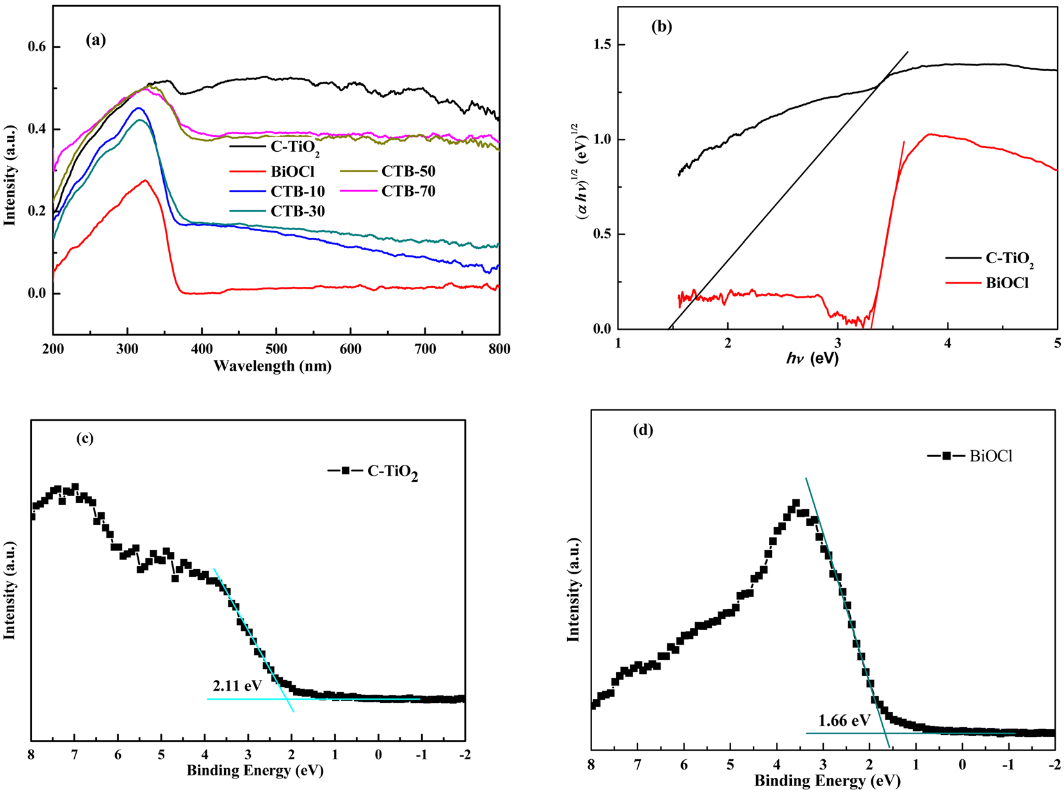

Fig. 5 (a) UV-vis DRS profiles and (b) E_g values obtained for the C-TiO_2 and BiOCl. Valence band (VB) XPS profiles for the (c) C-TiO_2 and (d) BiOCl composites.

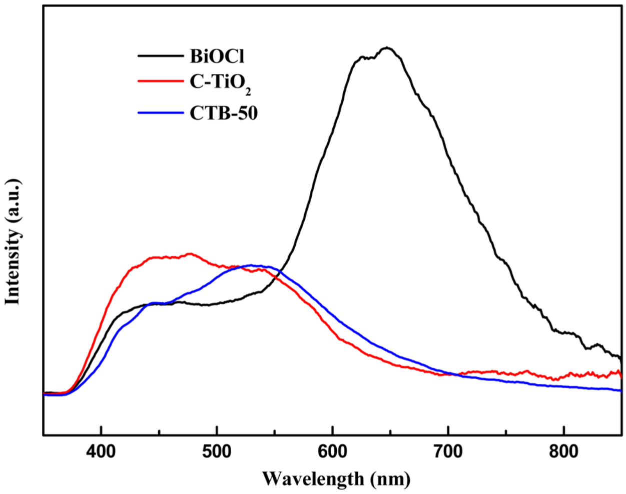

Fig. 6 PL profiles obtained for the C-TiO$_2$, BiOCl, and CTB-50 composites.

existence of Bi^{3+} ions within BiOCl,[14,41,42] with no peaks detected for impurities, indicating the high purity of BiOCl. The signals at 198.03 (Cl $2p_{3/2}$) and 199.68 eV (Cl $2p_{1/2}$) within the Cl 2p spectrum (Fig. 3(f)) corresponded to Cl^- ions.[43]

BET analysis of C-TiO$_2$/BiOCl composites

The pore size distribution curves and N_2 desorption/adsorption isotherms of the materials are presented in Fig. 4, and the Brunauer–Emmett–Teller (BET) surface area and pore size values are listed in Table 1. BiOCl exhibited a relatively small specific surface area (1.334 $m^2\ g^{-1}$) because of its nanosheet structure. After compositing with C-TiO$_2$, the surface area increased to some extent, with CTB-50 showing a value between those of C-TiO$_2$ and BiOCl. Based on the experimental results of this photocatalytic degradation of TCH, the specific surface area has a relatively small effect on photocatalytic activity.

TiO_2 displayed a relatively large pore size, whereas BiOCl and CTB-50 presented smaller pore sizes. Judging from the data and in combination with the pore size distribution curve, it can be inferred that the pore characteristics are slit pores produced by lamellar accumulation.

Photoelectric properties of the C-TiO$_2$/BiOCl composites

The UV-vis DRS plots obtained for the prepared materials are presented in Fig. 5(a). After calcination at 400 °C, the prepared C-TiO$_2$ derived from $Ti_3C_2T_x$ still contained a small amount of reduced Ti species, such as Ti_xO_y, indicating that it retained certain characteristics of $Ti_3C_2T_x$. As a result, it exhibited strong absorption characteristics within the UV-vis region. BiOCl displayed an absorption edge at about 370 nm.[44,45] After compositing with C-TiO$_2$, the absorption of BiOCl within the visible-light region was substantially enhanced. When the proportion of C-TiO$_2$ reached 50%, the absorption edge of the prepared composite underwent a clear redshift, resulting in a substantial increase in visible-light absorption.

The energy band gap (E_g) calculation of the samples was carried out *via* the Kubelka–Munk equation based on data extracted from the UV-vis DRS:[46]

$$\alpha h\nu = A(h\nu - E_g)^{n/2} \tag{1}$$

where α denotes the absorption coefficient, ν indicates the incident light frequency, h represents Planck's constant, E_g denotes the energy band gap, and A represents a constant (taken as 1). The values of n for indirect and direct bandgap semiconductors are 4 and 1, respectively.[47] Since both anatase TiO_2 and tetragonal BiOCl are classified as indirect bandgap semiconductors, $n = 4$ was applied for both.[14,46] By plotting $(\alpha h\nu)^{1/2}$ against $h\nu$, the slope of the tangent line at the point where $\alpha = 0$ corresponds to the energy band gap E_g.[48] The experimental results are provided in Fig. 5(b). The bandgap of C-TiO$_2$ was measured at 1.47 eV, and the BiOCl energy bandgap was determined to be 3.31 eV.[25,45]

To further investigate photogenerated electron–hole pair recombination, PL measurements of the prepared samples were recorded, as presented in Fig. 6. BiOCl has the strongest PL spectrum, indicating that it has the highest degree of electron–hole recombination. After compounding with C-TiO$_2$, the PL spectrum of the composite material CTB-50 significantly decreases compared with that of BiOCl, demonstrating that photogenerated electron–hole pairs separate efficiently and effectively suppress their recombination.[49] Transient photocurrent response and electrochemical impedance

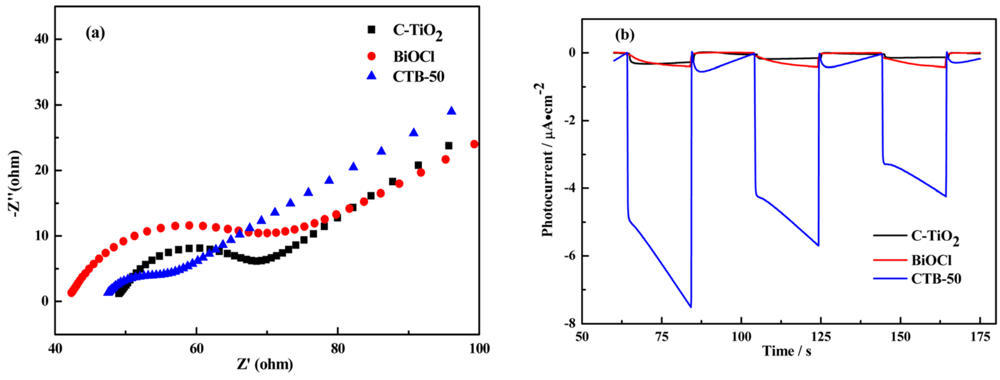

Fig. 7 (a) EIS Nyquist plot and (b) transient photocurrent response plots obtained for the C-TiO$_2$, BiOCl, and CTB-50 composite materials.

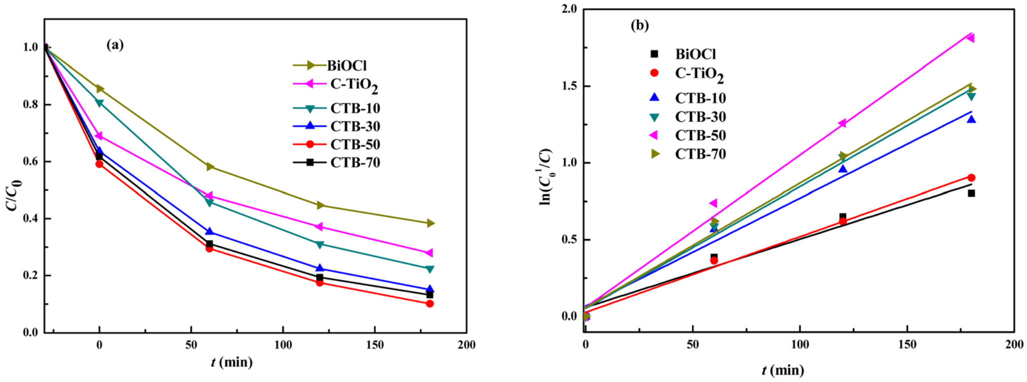

Fig. 8 (a) Photocatalytic degradation and (b) kinetic graphs of TCH degradation by C-TiO_2/BiOCl composites.

Table 2 Comparison of the photocatalytic degradation efficiency of TCH with that of other photocatalysts reported in the literature

Materials	Dosage of catalyst	Concentration of TCH (mg L^{-1})	Illumination time (min)	Degradation rate (%)	Reaction conditions	Ref.
SnS_2/TiO_2	1.5 cm^2	10	90	93.4	300 W Xe lamp	51
$SrTiO_3/Ti_3C_2T_x$	—	30	30 min	93.7	PMS synergism	52
TiO_2-5	0.3 g L^{-1}	20	60	89	Xenon lamp	4
$(BiO)_2CO_3$/BiOCl	1 g L^{-1}	10	60	95.3	Visible light	18
BiOCl	20 mg	20	120	86	300 W Xe lamp	32
BiOCl/TiO_2/sepiolite	60 mg	50	180	91.8	400 W Xe lamp	53
Palygorskite-supported Cu_2O–TiO_2	1 g L^{-1}	30 mg L^{-1}	240	88.81	500 W Xe lamp	54
BiOCl/Bi_2WO_6	20 mg	20 mg L^{-1}	150	63.9	300 W Xe lamp	55
C-TiO_2/BiOCl	1 g L^{-1}	20	180	89.9	350 W Xe lamp	This work

spectroscopy (EIS) characterizations were also conducted on the CTB-50 composite material to evaluate the effect of the C-TiO_2/BiOCl composite on photogenerated carrier separation and transfer. Fig. 7 shows the results. The EIS Nyquist plot in Fig. 7(a) shows that the semicircle of CTB-50 is smaller than those of C-TiO_2 and BiOCl, indicating a faster electron migration rate in CTB-50.[50] Compared with C-TiO_2 and BiOCl, the CTB-50 composite results in a markedly higher photocurrent density, as illustrated in Fig. 7(b), further confirming that CTB-50 results in superior and more rapid photogenerated charge separation and migration efficiency than C-TiO_2 and BiOCl.[36]

Photocatalytic efficiency of the C-TiO_2/BiOCl samples

With a 1 g L^{-1} photocatalyst dosage and an initial TCH concentration of 20 mg L^{-1}, a 30-min dark reaction was first carried out. The TCH photocatalytic degradation by the C-TiO_2/BiOCl samples was subsequently investigated under irradiation from a 350 W Xe lamp, and the results are shown in Fig. 8(a). According to the data presented in Fig. 8(a), higher

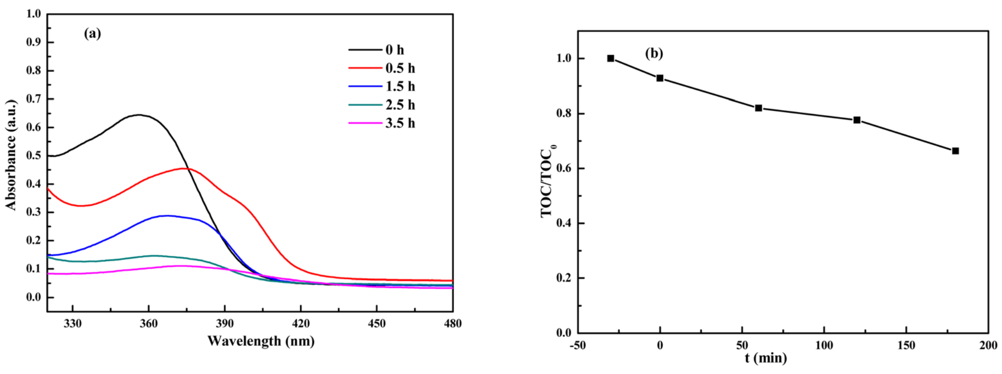

Fig. 9 Curves obtained for the photocatalytic degradation process of TCH (a) and the total organic carbon (TOC) curve throughout the process of degradation by the CTB-50 composite photocatalyst (b).

Table 3 PFOK kinetic rate constants and correlation coefficients for TCH degradation by C-TiO_2/BiOCl composites

Materials	Kinetic rate constants (k, min^{-1})	Correlation coefficients (R^2)
BiOCl	0.00445	0.944
C-TiO_2	0.00493	0.992
CTB-10	0.00704	0.974
CTB-30	0.00794	0.988
CTB-50	0.00992	0.990
CTB-70	0.00812	0.986

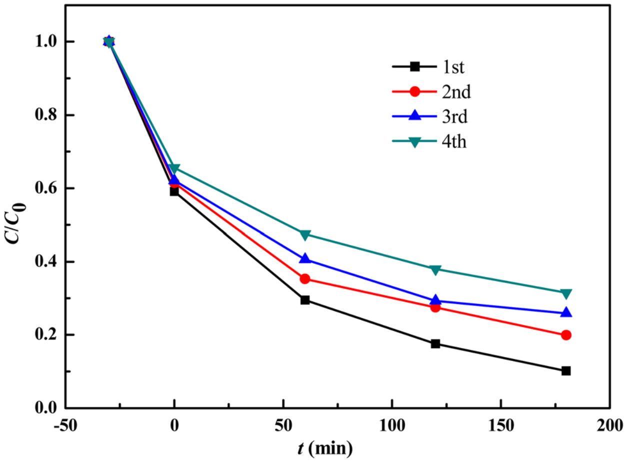

Fig. 10 Repeated experiments on the degradation of TCH by the CTB-50 composite photocatalyst.

photocatalytic activity was observed for the C-TiO_2/BiOCl composites toward TCH than for the pure BiOCl and C-TiO_2 composites. Among them, the CTB-50 composite photocatalyst, with a C-TiO_2 proportion of 50%, exhibited the highest degradation rate of TCH, reaching 89.9% within 3 h. Table 2 compares the activity of the CTB-50 photocatalytic material with that of various photocatalytic materials reported in the literature in the degradation process of TCH. The photocatalytic activity of CTB-50 is comparable to that of other photocatalytic materials reported in the literature.

The UV-vis absorption profiles of TCH during its degradation by CTB-50 are presented in Fig. 9(a). The absorption peak of TCH continuously decreases as the reaction progresses, indicating the gradual degradation of TCH. To further evaluate mineralization, the total organic carbon (TOC) content during TCH degradation was measured, as shown in Fig. 9(b). After 3 h of photocatalytic degradation, the TOC removal rate was 33.6%, which was considerably lower than the TCH degradation rate. This suggests that while TCH molecules were degraded, they were not completely mineralized.

The photocatalytic degradation of TCH by the C-TiO_2/BiOCl composites was further analyzed *via* the pseudo-first-order kinetic (PFOK) model, and the results are presented in Fig. 8(b). The corresponding linear correlation coefficients and kinetic rate constants are summarized in Table 3. As shown in Table 3 and illustrated in Fig. 8(b), the linear correlation coefficients are close to 1. This suggested that the photocatalytic degradation process generally follows PFOK kinetics. The reaction rate was enhanced after combining C-TiO_2 with BiOCl. Among all the samples, CTB-50 demonstrated the highest rate constant of 0.00992 min^{-1}, which was about twice that of C-TiO_2 and 2.2 times that of BiOCl. Thus, the TCH degradation efficiency was significantly improved by the composite photocatalyst.

High photocatalyst stability and good reusability are essential for their industrial applicability. To this end, the reuse performance of the CTB-50 photocatalyst, which exhibited the best degradation effect, was evaluated, and its SEM image and XRD patterns before and after use were compared. The results are presented in Fig. 10 and 11, respectively. After being reused four times, the CTB-50 photocatalyst achieved a 68.5% degradation rate for TCH, indicating a certain degree of decline in efficiency. As shown in Fig. 11, no noticeable changes were observed in the SEM image and main characteristic peaks of XRD patterns of CTB-50 before and after use, indicating that CTB-50 maintained good stability.

Mechanism of photocatalytic degradation of TCH by C-TiO_2/BiOCl composites

To identify the production of primary active species during the photocatalytic process, isopropyl alcohol (IPA), ammonium

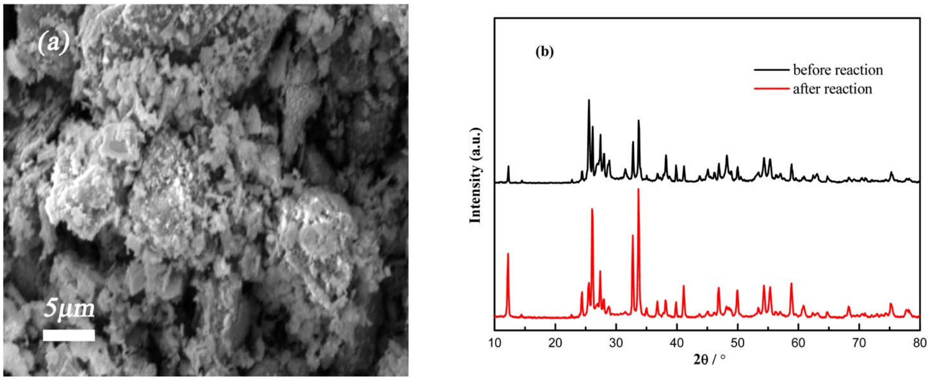

Fig. 11 (a) SEM image and (b) XRD patterns of CTB-50 after four cycles of reuse.

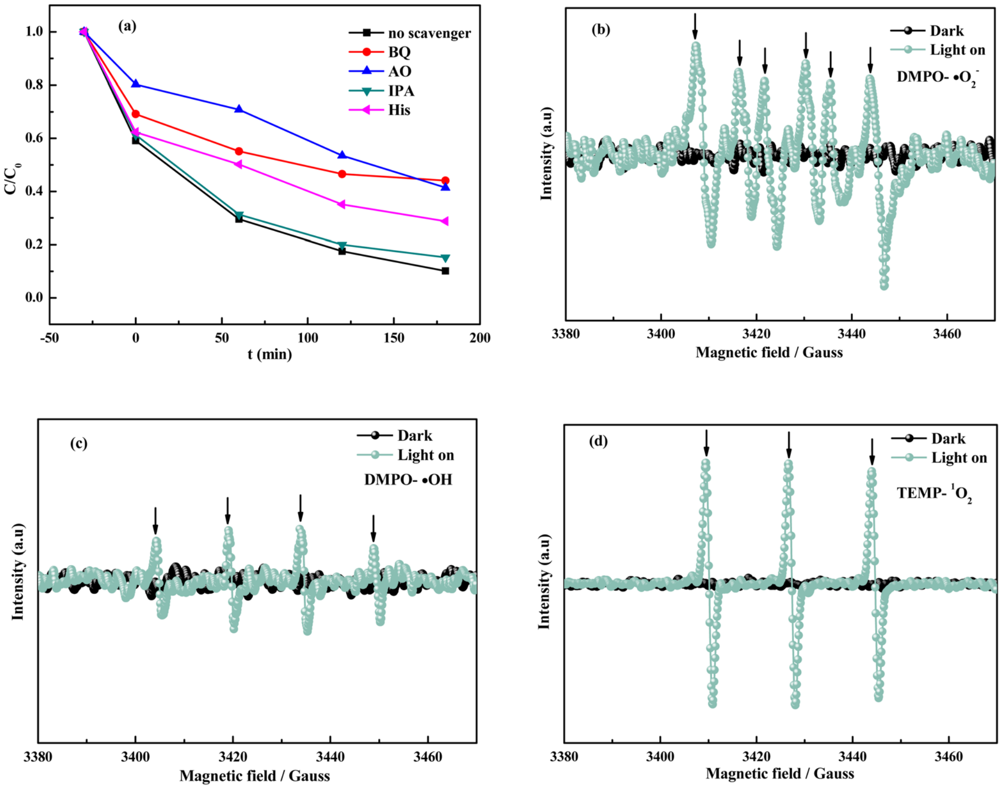

Fig. 12 (a) Effects of scavengers on TCH degradation by CTB-50; (b) DMPO spin-trapping EPR spectrum of CTB-50 in a CH_3OH dispersion ($^{\bullet}O_2^-$), (c) DMPO spin-trapping EPR spectrum in water ($^{\bullet}OH$), and (d) TEMP spin-trapping EPR spectrum in water ($^1O_2$).

oxalate (AO), *p*-benzoquinone (BQ), and L-histidine (His) were utilized as scavengers for holes (h^+), superoxide radicals ($^{\bullet}O_2^-$), hydroxyl radicals ($^{\bullet}OH$), and singlet oxygen ($^1O_2$), respectively, in the degradation of TCH by CTB-50. The impact of these scavengers on the photocatalytic process is illustrated in Fig. 12(a). The degradation rate of TCH decreased most substantially following the addition of BQ and AO, suggesting that h^+ and $^{\bullet}O_2^-$ played dominant roles in TCH photocatalytic degradation by CTB-50. The degradation rate also decreased to some extent after the addition of His, suggesting that $^1O_2$ contributes to the degradation process. Conversely, the introduction of IPA had little effect, suggesting that $^{\bullet}OH$ played a relatively minor role. Electron paramagnetic resonance (EPR) tests were conducted to detect $^{\bullet}O_2^-$, $^{\bullet}OH$, and $^1O_2$ radicals after 10 min of exposure to a xenon lamp to further verify the production of radicals. The results are shown in Fig. 12(b)–(d). Distinct detection peaks for $^{\bullet}O_2^-$ and $^1O_2$ were observed after illumination. Compared with the strong peak for $^1O_2$, the peak for $^{\bullet}OH$ was relatively weak. This is attributed to the lower conversion potential of $O_2/^1O_2$ (1.88 eV *vs.* NHE)[56] than that of $^{\bullet}OH/OH^-$ (1.99 eV *vs.* NHE),[57] making the formation of $^1O_2$ more favorable. These EPR results were consistent with those of the radical scavenger experiments.

Combining the energy band data of C-TiO_2 and BiOCl with the radical trapping results, a Z-scheme heterojunction catalytic mechanism is proposed (Fig. 13) for the TCH photocatalytic degradation induced by the C-TiO_2/BiOCl composite, with the carbon layer acting as a mediator. Under light excitation, the conduction band electrons (e^-) of BiOCl (−1.66 eV, more negative than −0.33 eV for $O_2/^{\bullet}O_2^-$ (ref. 56)) reduce O_2 to $^{\bullet}O_2^-$ radicals. The valence band holes (h^+) of C-TiO_2 (2.11 eV, more positive than 1.88 eV for $O_2/^1O_2$ (ref. 57)) oxidize O_2 to $^1O_2$ radicals. Both h^+, $^{\bullet}O_2^-$, and $^1O_2$ exhibit strong oxidizing abilities, leading to the degradation of TCH. The C-TiO_2 conduction band electrons recombine with the valence band holes of BiOCl

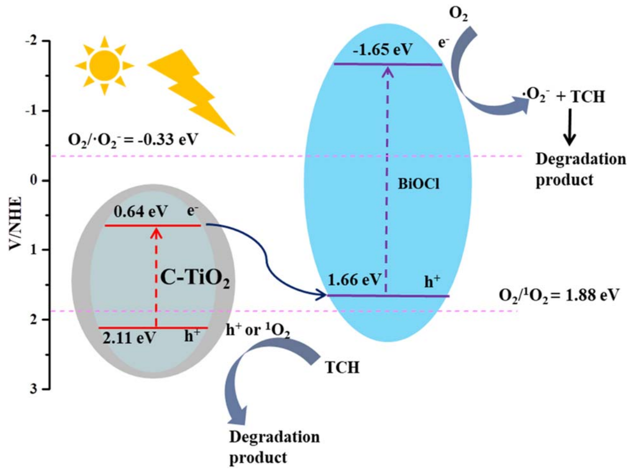

Fig. 13 Proposed catalytic degradation mechanism of TCH by the C-TiO_2/BiOCl composite photocatalyst.

through the carbon layer mediator, effectively suppressing the recombination of electron–hole pairs and thereby enhancing the photocatalytic efficiency. Wu *et al.*[58] reported a similar mechanism for a TiO_2/g-C_3N_4 Z-scheme photocatalyst supported by a graphene layer prepared from $Ti_3C_2T_x$ and melamine.

Conclusion

By calcining $Ti_3C_2T_x$, carbon-doped anatase TiO_2 was successfully prepared as the main product. The relatively low calcination temperature retained a small amount of reduced Ti ions (Ti_xO_y), preserving some metallic properties of $Ti_3C_2T_x$ and enabling the resulting C-TiO_2 to exhibit enhanced absorption in the range covering the visible light. When combined with BiOCl, a C-TiO_2/BiOCl composite photocatalyst was obtained. This study investigated the effect of different C-TiO_2/BiOCl ratios on the photocatalytic degradation of TCH. At a 50% C-TiO_2 to BiOCl ratio (CTB-50), the photocatalyst achieved an 89.9% degradation rate of TCH after 3 h of illumination.

Energy band analysis indicated the generation of a carbon-mediated Z-scheme heterojunction between C-TiO_2 and BiOCl. PL spectroscopy and electrochemical tests demonstrated that the composite efficiently restricted the recombination of photogenerated hole/electron pairs and improved their transportation and separation. Radical trapping and EPR tests revealed that holes (h^+) and superoxide radicals ($^{\bullet}O_2^-$) were the main active species, while singlet oxygen ($^1O_2$) also contributed to the degradation process. Reuse experiments confirmed the remarkable stability of the C-TiO_2/BiOCl composite photocatalyst, highlighting its suitability for practical applications in treating antibiotic-contaminated and other pollutant-rich wastewater.

Author contributions

Conceptualization: Fang-Di Wu, Jyh-Cherng Chen; methodology: Fang-Di Wu, Jyh-Cherng Chen; investigation: Fang-Di Wu, Shuang Yang, Ao-xue Fang; writing – original draft: Fang-Di Wu, Shuang Yang, Ao-xue Fang; writing – review and editing: Fang-Di Wu, Jyh-Cherng Chen; funding acquisition: Fang-Di Wu.

Conflicts of interest

The authors declare that they have no conflict of interest.

Data availability

The data supporting this study are available from the corresponding author upon reasonable request.

Acknowledgements

This work was supported by the project of National Science Foundation for Fujian Province, China (2025J011072), the Introduced Talent Start-up Fund Project of Wuyi University (YJ202323), Science and Technology Innovation Development Fund of Wuyi University (2021J011139+N2021J005-2N2021J005-2) and the Project of Fujian Provincial College Students' Innovation and Entrepreneurship Training Program (S202410397056).

References

1 S. Li, X. Li, Y. Liu, P. Zhang, J. Zhang and B. Zhang, *Chin. J. Catal.*, 2025, **72**, 130–142.
2 S. Li, X. Wang, B. Xue, D. Feng, Y. Liu and W. Jiang, *J. Mater. Sci. Technol.*, 2026, **246**, 237–246.
3 C. Wang, K. Rong, Y. Liu, F. Yang and S. Li, *Sci. China Mater.*, 2024, **67**(2), 562–572.
4 Y. Li, H. Liu, C. Hou, Y. Xie, L. Wang and M. Zhang, *J. Alloys Compd.*, 2024, **970**, 172644.
5 M. S. Javed, M. A. Nazir, Z. Shafiq, S. Ullah, T. Najam, R. Iqbal, M. A. Ismail, T. L. Tamang and S. S. A. Shah, *J. Alloys Compd.*, 2025, **1010**, 177926.
6 W. Li, G. Liao, W. Duan, F. Gao, Y. Wang, R. Cui, X. Wang and C. Wang, *Appl. Catal., B: Environ. Energy*, 2024, **354**, 124108.
7 J. O. Adeyemi, T. Ajiboye and D. C. Onwudiwe, *Water, Air, Soil Pollut.*, 2021, **232**, 219.
8 Y. Wang, W. Li, W. Duan, R. Cui, G. Liao and N. Wang, *Chem. Eng. J.*, 2025, **519**, 165220.
9 A. Sridevi, B. R. Ramji, P. G. K. D. Venkatesan, V. Sugumaran and P. Selvakumar, *Inorg. Chem. Commun.*, 2021, **130**, 108715.
10 R. He, S. Cao, P. Zhou and J. Yu, *Chin. J. Catal.*, 2014, **35**(7), 989–1007.
11 D. Sun, J. Li, Z. Feng, L. He, B. Zhao, T. Wang, R. Li, S. Yin and T. Sato, *Catal. Commun.*, 2014, **5**, 1–4.
12 L. Mao, H. Liu, L. Yao, W. Wen, M.-M. Chen, X. Zhang and S. Wang, *Chem. Eng. J.*, 2022, **429**, 132297.
13 S. Li, R. Li, K. Dong, Y. Liu, X. Yu, W. Li, T. Liu, Z. Zhao, M. Zhang, B. Zhang and X. Chen, *Chin. J. Catal.*, 2025, **76**, 37–49.
14 G. Zhang, Y. Tan, Z. Sun and S. Zheng, *J. Environ. Chem. Eng.*, 2017, **5**, 1196–1204.
15 L. Song, Y. Pang, Y. Zheng and L. Ge, *Appl. Phys. A: Mater. Sci. Process.*, 2017, **123**, 500.
16 J.-Q. Chang, Y. Zhong, C.-H. Hu, J.-L. Luo and P.-G. Wang, *Inorg. Chem. Commun.*, 2018, **96**, 145–152.
17 H. Wang, S. Sun, M. Ding, J. Cui and S. Liang, *Chemosphere*, 2023, **329**, 138643.
18 H. Wang, S. Sun, M. Ding, J. Li, J. Lyu, S. Liang and J. Cui, *J. Environ. Chem. Eng.*, 2024, **12**, 112723.
19 J. Ding, G. Su, Y. Zhou, H. Yin, S. Wang, J. Wang and W. Zhang, *Environ. Pollut.*, 2024, **341**, 122942.
20 Y. Park, W. Kim, H. Park, T. Tachikawa, T. Majima and W. Choi, *Appl. Catal., B*, 2009, **91**, 355–361.
21 W. Ren, Z. Ai, F. Jia, L. Zhang, X. Fan and Z. Zou, *Appl. Catal., B*, 2007, **69**, 138–144.
22 M. Hou, J. Gao, L. Yang, S. Guo, T. Hu and Y. Li, *Appl. Surf. Sci.*, 2021, **535**, 147666.

23 X. Feng, Z. Yu, Y. Sun, R. Long, M. Shan, X. Li, Y. Liu and J. Liu, *Ceram. Int.*, 2021, **47**, 7321–7343.

24 X. Han, L. An, Y. Hu, Y. Li, C. Hou, H. Wang and Q. Zhang, *Appl. Catal., B*, 2020, **265**, 118539.

25 D. Sun, J. Li, L. He, B. Zhao, T. Wang, R. Li, S. Yin, Z. Feng and T. Sato, *CrystEngComm*, 2014, **16**, 7564–7574.

26 F.-D. Wu, J.-C. Chen and Z.-T. Yang, *New J. Chem.*, 2022, **46**, 10191–10200.

27 E. O. Oseghe and A. E. Ofomaja, *J. Environ. Manage.*, 2018, **223**, 860–867.

28 L. Ding, R. Wei, H. Chen, J. Hu and J. Li, *Appl. Catal., B*, 2015, **172–173**, 91–99.

29 L. Bao and Y.-J. Yuan, *Dalton Trans.*, 2020, **49**, 11536–11542.

30 X. Shi, L. Wang, A. A. Zuh, Y. Jia, F. Ding, H. Cheng and Q. J. Wang, *Alloy. Compd.*, 2022, **903**, 163889.

31 Y. Cai, D. Li, J. Sun, M. Chen, Y. Li, Z. Zou, H. Zhang, H. Xu and D. Xia, *Appl. Surf. Sci.*, 2018, **439**, 697–704.

32 Q. Zhou, Z. Ji, H. Yu, S. Lu, J. Guo and C. Wu, *Langmuir*, 2024, **40**, 7078–7086.

33 Z. Wu, Y. Liang, X. Yuan, D. Zou, J. Fang, L. Jiang, J. Zhang, H. Yang and Z. Xiao, *Chem. Eng. J.*, 2020, **394**, 124921.

34 T. Ke, S. Shen, K. Rajavel, K. Yang and D. Lin, *J. Hazard. Mater.*, 2021, **402**, 124066.

35 X. Han, L. An, Y. Hu, Y. Li, C. Hou, H. Wang and Q. Zhang, *Appl. Catal., B*, 2020, **265**, 118539.

36 Y. Yang, Z. Zeng, G. Zeng, D. Huang, R. Xiao, C. Zhang, C. Zhou, W. Xiong, W. Wang, M. Cheng, W. Xue, H. Guo, X. Tang and D. He, *Appl. Catal., B*, 2019, **258**, 117956.

37 B. M. Almeida, M. A. M. Jr, J. Bettini, J. E. Benedetti and A. F. Nogueira, *Appl. Surf. Sci.*, 2015, **324**, 419–431.

38 Z. Luo, H. Jiang, D. Li, L. Hu, W. Geng, P. Wei and P. yang, *RSC Adv.*, 2014, **4**, 17797.

39 Y. Yang, D. Ni, Y. Yao, Y. Zhong, Y. Ma and J. Yao, *RSC Adv.*, 2015, **5**, 93635–93643.

40 T. An, C. Y. Dou, J. N. Ju, W. L. Wei and Q. Z. Ji, *Vacuum*, 2019, **164**, 405–410.

41 D. Ma, F. Liang, Q. Xue, Y. Liu, C. Zhuang and S. Li, *Acta Phys.-Chim. Sin.*, 2025, **41**, 100190.

42 S. Li, C. You, K. Rong, C. Zhuang, X. Chen and B. Zhang, *Advanced Powder Materials*, 2024, **3**, 100183.

43 J. Di, J. Xia, M. Ji, B. Wang, S. Yin, Q. Zhang, Z. Chen and H. Li, *ACS Appl. Mater. Interfaces*, 2015, **7**, 20111–20123.

44 J. Yang, T. Xie, C. Liu and L. Xu, *Nanomaterials*, 2018, **8**, 697.

45 D. Ma, J. Zhong, J. Li, L. Wang and R. Peng, *Appl. Surf. Sci.*, 2018, **443**, 497–505.

46 W. Dong, T. Xie, Z. Wu, H. Peng, H. Ren, F. Meng and H. Lin, *RSC Adv.*, 2021, **11**, 38894.

47 D. S. Rodríguez, M. G. M. Medrano, H. Remita and V. E. Barrios, *J. Environ. Chem. Eng.*, 2018, **6**, 1601–1612.

48 W. Li, Y. Tian, H. Li, C. Zhao, B. Zhang, H. Zhang, W. Geng and Q. Zhang, *Appl. Catal., A*, 2016, **516**, 81–89.

49 S. Weng, B. Chen, L. Xie, Z. Zheng and P. Liu, *J. Mater. Chem. A*, 2013, **1**, 3068.

50 B. Yang, J. Zheng, W. Li, R. Wang, D. Li, X. Guo, R. D. Rodriguez and X. Jia, *Dalton Trans.*, 2020, **49**, 11010–11018.

51 S. Ding, W. Gan, J. Guo, R. Chen, R. Liu, Z. Zhao, J. Li, M. Zhang and Z. Sun, *J. Mater. Chem. C*, 2024, **12**, 7079–7094.

52 X. Wu, J. Chen, X. Yang, H. Zheng, Y. Ma and Y. Li, *Appl. Surf. Sci.*, 2025, **680**, 161317.

53 X. Hu, Z. Sun, J. Song, G. Zhang, C. Li and S. Zheng, *J. Colloid Interface Sci.*, 2019, **533**, 238–250.

54 Y. Shi, Z. Yang, B. Wang, H. An, Z. Chen and H. Cui, *Appl. Clay Sci.*, 2016, **119**, 311–320.

55 R. Peng, Y. Kang, X. Deng, X. Zhang, F. Xie, H. Wang and W. Liu, *J. Environ. Chem. Eng.*, 2021, **9**, 106750.

56 Y. Zhou, M. Yu, H. Liang, J. Chen, L. Xu and J. Niu, *Appl. Catal., B*, 2021, **291**, 120105.

57 Q. Wang, W. Wang, L. Zhong, D. Liu, X. Cao and F. Cui, *Appl. Catal., B*, 2018, **220**, 290–302.

58 Z. Wu, Y. Liang, X. Yuan, D. Zou, J. Fang, L. Jiang, J. Zhang, H. Yang and Z. Xiao, *Chem. Eng. J.*, 2020, **394**, 124921.